A SIMPLIFIED EMPIRICAL LINE CALIBRATION METHOD FOR sUAS-BASED REMOTE SENSING

Chuyuan Wang
Soe W. Myint
School of Geographical Sciences and Urban Planning
Arizona State University, Tempe, AZ 85287, USA
chuyuanw@asu.edu
soe.myint@asu.edu

Kevin P. Price
RoboFlight Systems, LLC.
5530 West Parkway, Suite 300, Johnston, IA 50131, USA
kevin@roboflight.com

Huan Wang
Nan An
Department of Agronomy
Kansas State University, Manhattan, KS 66506, USA
ksuwanghuan@ksu.edu
nanan@ksu.edu

ABSTRACT

The use of small unmanned aircraft systems (sUAS) to acquire very high resolution multispectral imagery has attracted growing attention recently; however, no feasible and convenient radiometric calibration method has been specifically developed for sUAS remote sensing. In this research we used a modified color infrared (CIR) digital single-lens reflex (DSLR) camera as the sensor and the DJI S800 hexacopter sUAS as the platform to collect imagery. Results show that the relationship between image raw digital numbers (DNs) and the natural logarithm of measured surface reflectance is linear and the *y*-intercept of the linear equation can be interpreted as the minimal surface reflectance that can be detected by each sensor waveband. The empirical line calibration equation for every single band image can be built using the *y*-intercept as one data point, and the natural log-transformed measured reflectance and image DNs of a gray calibration target as another point in the coordinate system. Image raw DNs are therefore converted to reflectance using the calibration equation. The Mann-Whitney *U* test results suggest that the difference between the measured and predicted reflectance values of thirteen tallgrass sampling quadrats is not statistically significant. The method theory developed in this study can be effectively employed for other sUAS-based remote sensing applications.

KEYWORDS: small unmanned aircraft systems, very high resolution, radiometric calibration, empirical line.

INTRODUCTION

Recently, growing attention has been given to the use of small unmanned aircraft systems (sUAS) as a viable alternative to conventional satellite and airborne platforms for acquiring very high spatial resolution multispectral imagery (Bland *et al.*, 2004; Everaerts, 2008; Nebiker *et al.*, 2008). Civilian and scientific applications of sUAS-base remote sensing technology have been mostly found in commercial aerial surveillance (Beard *et al.*, 2006), forest fire detection (Merino *et al.*, 2011), oil, gas and mineral exploration and production (Barnard, 2010), marine management (Veenstra and Churnside, 2012), meteorological research (Martin *et al.*, 2011), and cropland and rangeland management (Wang *et al.*, 2014; Hunt *et al.*, 2010). One advantage of using a sUAS platform is the derivation of very high spatial resolution imagery yielding pixels from less than one millimeter to a few centimeters in size that can provide very detailed photogrammetric information of the surface. Another advantage is that a sUAS can be flown whenever weather conditional is favorable thus providing very high temporal resolution imagery for

the target area of interest. In addition, sUAS offers advantage in safety, particularly when dealing with land surveys in very difficult terrain.

Remotely sensed imagery may contain noise or error from the sensor system or the environment. Radiometric calibration is therefore a prerequisite in digital image processing, especially when imagery is acquired for biophysical analysis, change detection across date, and comparison across sensor.

Radiometric calibration for digital photogrammetric systems using very large test field has been studied (Honkavaara *et al.*, 2010). This method is applicable to calibrate image sensors, large-scale high resolution satellite imagery and airborne imagery collected by a pilot navigated aircraft at very high altitudes. Since sUAS flight altitude is much lower and the image dimension is much smaller, this method is not feasible to calibrate sUAS imagery.

The use of empirical line method to calibrate remotely sensed data to surface reflectance is one of the most widely used methods for airborne imagery as it is straightforward and effective to be implemented (Smith and Milton, 1999). Most researchers used two calibration targets of different gray levels and developed a workflow to calibrate the imagery (Kruse *et al.*, 1990; Ben-Dor *et al.*, 1994; Van der Meer, 1994; Dwyer *et al.*, 1995; Ferrier and Wadge, 1996; Laliberte *et al.*, 2011). Some used four targets to improve the calibration accuracy (Farrand *et al.*, 1994; Price *et al.*, 1995). No matter how many targets were used in those studies, they all assumed the relationship between surface reflectance and at-sensor radiance is linear. Therefore, the light and dark colored calibration targets were used to build linear calibration equations to convert at-sensor radiance to estimated surface reflectance for each sensor waveband. This calibration method may be acceptable for other studies, but many problems have been. One common issue is that at-sensor radiance data are not readily available for all the airborne images. Some studies used image raw digital numbers (DNs) instead of at-sensor radiance to build calibration equations (Leliberte *et al.*, 2011), despite the fact that the relationship between surface reflectance and image raw DNs is not always linear (Stow *et al.*, 1996). Commercial digital cameras have become widely used in land survey and photogrammetric analysis because they are cost-effective and easier to operate; however, most digital cameras have built-in algorithms that use a curvilinear function to transform electromagnetic radiation (EMR) to digital signals as the way human eyes perceive grayness. The purpose is to take nice-looking pictures, but not scientific data for research. Therefore, the relationship between surface reflectance and image raw DNs remains unknown for these cameras.

Due to the technical limitations of all the calibration methods aforementioned, a feasible and convenient radiometric calibration method needs to be specifically developed for the imagery collected by commercial digital cameras using sUAS. The first objective of this research is to discover the relationship between measured surface reflectance and image raw DNs. The second objective is to develop a systematic radiometric calibration method for sUAS remote sensing based on the analysis results from the first procedure. The third objective is to validate the effectiveness of this newly developed calibration method.

MATERIALS AND PROCEDURES

Sensor

The sensor used throughout this research is the Canon EOS Rebel T4i digital single-lens reflex (DSLR) camera with a Canon L-series 24-mm lens. This camera was modified by LDP LLC (*http://www.maxmax.com*) to collect color infrared (CIR) digital imagery in the green, red and near-infrared (NIR) portions of the spectrum. Detailed camera specifications and spectral waveband information are summarized in Table 1.

Table 1. Specifications of the modified Canon EOS Rebel T4i digital camera.

Sensor type	Effective pixels (megapixels)	Pixel unit (μm^2)	Full width at half maximum (FWHM) (nm)	Peak wavelength (nm)
CMOS	18.0	4.3	Green: 530-590 Red: 590- 680 NIR: 807-867	Green: 552 Red: 638 NIR: 833

Gray Gradient Calibration Panel

A gray gradient calibration panel will be used to study the relationship between surface reflectance and image raw DNs. We have tested more than 10 different materials readily available in the market that are cost-efficient and easy to transport, and finally found the Masonite hardboard with a rough surface has the optimal radiometric property that meets our need. A calibration panel was made using one whole 244 cm × 61 cm × 0.32 cm (96" × 24" × 1/8", L × W

× H) Masonite hardboard and was painted at least 0.5 mm thick using a gray gradient of 9 different levels from 5% to 90%.

We tested the radiometric property of the Masonite hardboard surface for all the gray levels in a clear sunny day at around solar noon using the Analytical Spectral Devices, Inc. (ASD) FieldSpec 3 spectroradiometer to take spectral measurements at a fixed altitude from 10 different viewing angles 360 degrees around. Reflectance values are calculated for the wavelengths between 500 nm and 900 nm that cover the spectral region of the three camera wavebands. To give an example, the reflectance curves captured from all the 10 viewing angles for the 30% gray level are shown in Figure 1. A one-way analysis of variance (ANOVA) is used to test the null hypothesis (H_0) that all the 10 reflectance means are the same. The test result shows a calculated F-statistic value of 1.62 ($p > 0.05$) (Table 2), suggesting that we fail to reject H_0. The same test result is also obtained for all the other gray levels. It indicates the Masonite hardboard surface is highly Lambertian. Hence, it can be considered as a suitable material for the radiometric calibration target for this research.

The mean reflectance curves for all the gray levels are shown in Figure 2. It demonstrates that reflectance value decreases as percent gray value increases. The mean reflectance value of each gray level for the spectral region of each camera wavebands was plotted against the percent gray value (Figure 3), and an exponential relationship was found between these two variables (Table 3). These regression models can be used to estimate the mean reflectance of a given percent gray value.

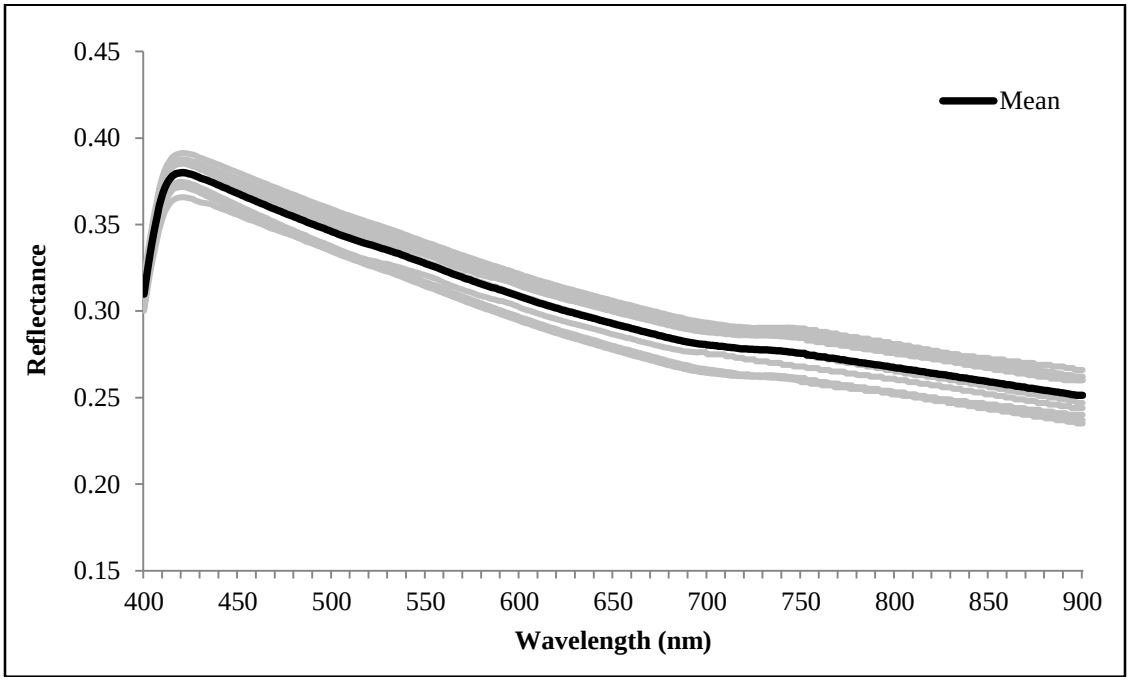

Figure 1. Reflectance curves of the Masonite hardboard painted with 30% gray level captured from 10 different viewing angles. The dark black line indicates the mean reflectance curve.

Table 2. One-way ANOVA test for reflectance values of 30% gray level.

Source	Sum of squares	Degrees of freedom	Mean sum of squares	F-statistic	Critical F-value ($\alpha = 0.05$)	p-value
Between groups	0.021580	9	0.002398	1.62	1.88	0.1057
Within groups	7.414008	5000	0.001483			
Total	7.435588	5009	-			

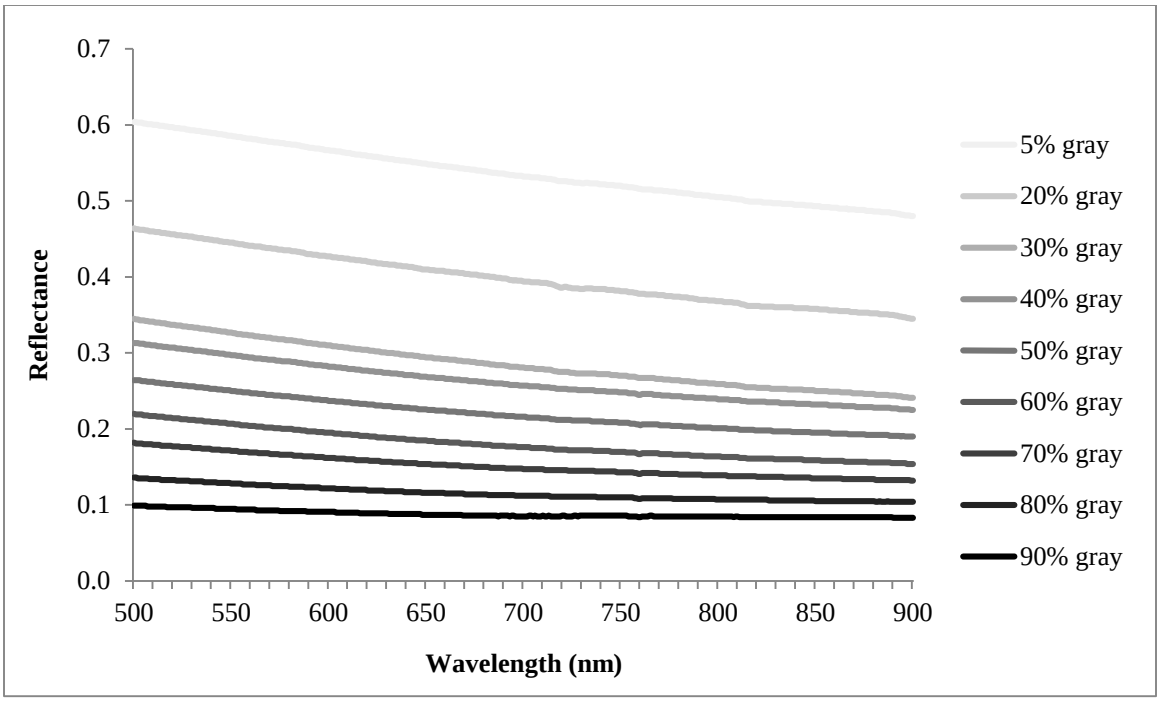

Figure 2. Mean reflectance curves for all gray levels.

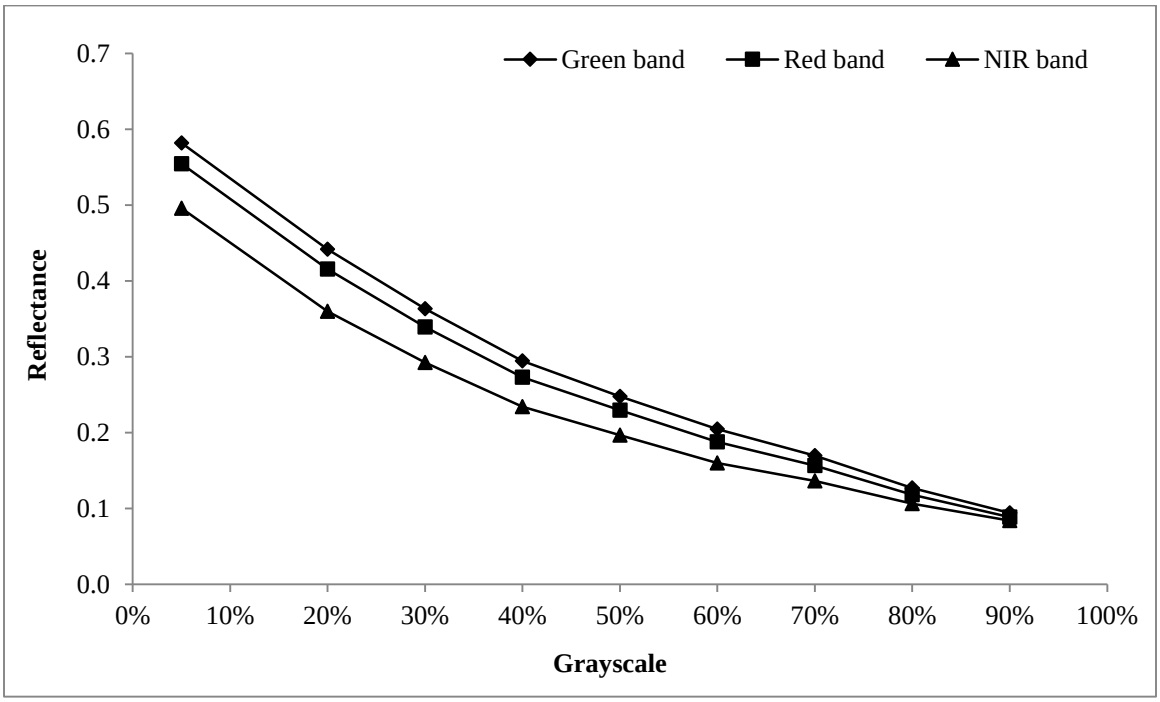

Figure 3. The relationship between percent gray value and their corresponding mean reflectance at the spectral region of each sensor wavebands.

Table 3. Regression analysis between percent gray values and mean reflectance values.

Camera waveband	Regression equation	Goodness-of-fit (r^2)
Green	$y = 0.676\exp(-2.081x)$	0.992 (p<0.01)
Red	$y = 0.637\exp(-2.101x)$	0.995 (p<0.01)
NIR	$y = 0.544\exp(-2.044x)$	0.999 (p<0.01)

* Note: x represents the percent gray value and y represents mean reflectance.

sUAS Platform and Image Acquisition

The sUAS used to carry the camera is the "Spreading Wings" S800 hexacopter made by DJI Innovations (Figure 4). This sUAS is well adapted for flying slow over fixed locations at low altitudes. It can lift a payload of 2.5 kg for an overflight of around 15 minutes under a calm weather condition.

The camera was installed on the hexacopter gimbal system to collect imagery in the Canon raw digital format (*.cr2) for the gray gradient calibration panel at an altitude of 10 m above the ground at around solar noon. Images were collected from 9 different viewing angles 360 degrees around the panel (including Nadir). One sample CIR image is shown in Figure 5.

All the CIR images were converted into 8-bit Tagged Image File Format (TIFF) format using Digital Photo Professional (DPP) software. The central pixels of the same gray level from images of all the viewing angles were extracted, and the mean DNs were calculated and then plotted against the mean reflectance values at wavelengths of each camera waveband.

Interpretation and Manipulation of the Empirical Line Calibration Equations

Figure 6(a) shows scatter plots and regression models for all the three camera wavebands. The *x*-axis represents image raw DN and the *y*-axis is reflectance. It demonstrates that the relationship between image raw DN and surface reflectance for the modified Canon T4i digital camera is not linear but exponential ($r^2 > 0.99$, $p < 0.05$). A natural logarithm transformation was performed on the mean reflectance values of each gray level to convert exponential equations into linear. Figure 6(b) shows a linear relationship between DN and the natural log-transformed reflectance values for each camera waveband. Let x equal 0 for all the linear equations in Figure 6(b), and the y-intercept is 3.56 for the green band, 3.66 for the red band, and 3.79 for the NIR band. Convert the y-intercepts back to reflectance and we get 0.028, 0.026, and 0.023 for the green, red, and NIR band respectively. These values can be interpreted as the minimum reflectance from the surface that can be detected by each sensor waveband, which is the intrinsic property of this camera that does not vary as the external environmental conditions change. In other words, the y-intercept of each empirical line equation can be seen as a constant calibration parameter for each camera waveband. Reflectance of an object surface is an inherent physical property that does not change in a short time period, but image DNs of the object can change as external environment changes from time to time under the same camera settings. Consequently, the slope coefficient of an empirical line calibration equation will constantly change. It is therefore required to build one calibration equation for every single band image, but it's not technically viable to use such a large gray gradient calibration panel for every fieldwork, especially when collecting data for a large geographic area. We have to simplify this calibration procedure in order to make it easier to be implemented in the field when a large number of images need to be collected.

Simplification of the Radiometric Calibration Procedure

Since it has been proven that the relationship between image raw DNs and the natural log-transformed reflectance value is linear and the y-intercept of the calibration equation can be used as a constant calibration parameter for each waveband, we just need another data point in the coordinate system to construct a new calibration empirical line for every single band image. If that is the case, only one target of one gray level is required, which would make the calibration procedure significantly easier. More detailed steps are described as follows.

The first step is to construct several calibration targets using the Masonite board painted by the same gray level. The mean reflectance of the target at the wavelengths of each camera waveband can be estimated using regression equations in Table 3.

The second step is to collect imagery for these calibration targets and calculate their mean DNs from every single band image. These targets should be distributed in the field at an appropriate space interval according to the flying altitude of the sUAS and specifications of the camera being used so that to ensure at least one target will be shown in each image.

Figure 4. DJI S800 "Spreading Wings" hexacopter in its overflight carrying a modified Canon EOS Rebel T4i DSLR camera.

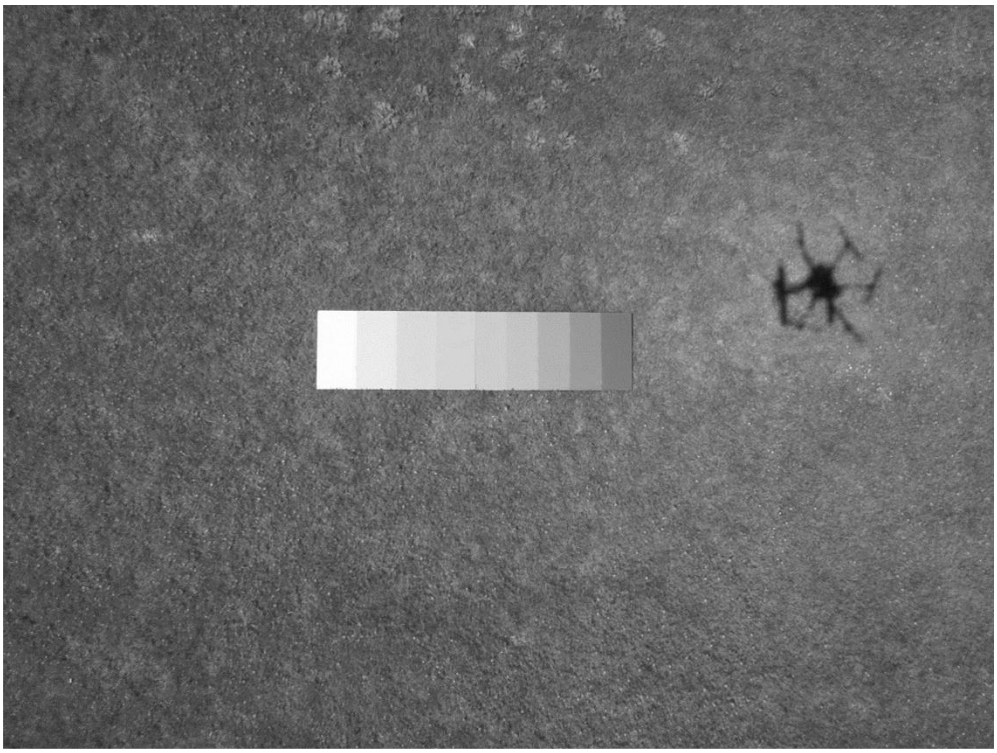

Figure 5. A sample CIR image of the gray gradient calibration panel. The gray level is 5%, 20%, 30%, 40%, 50%, 60%, 70%, 80%, and 90% respectively from the left to the right. The shadow cast on the ground is from the DJI S800 hexacopter sUAS.

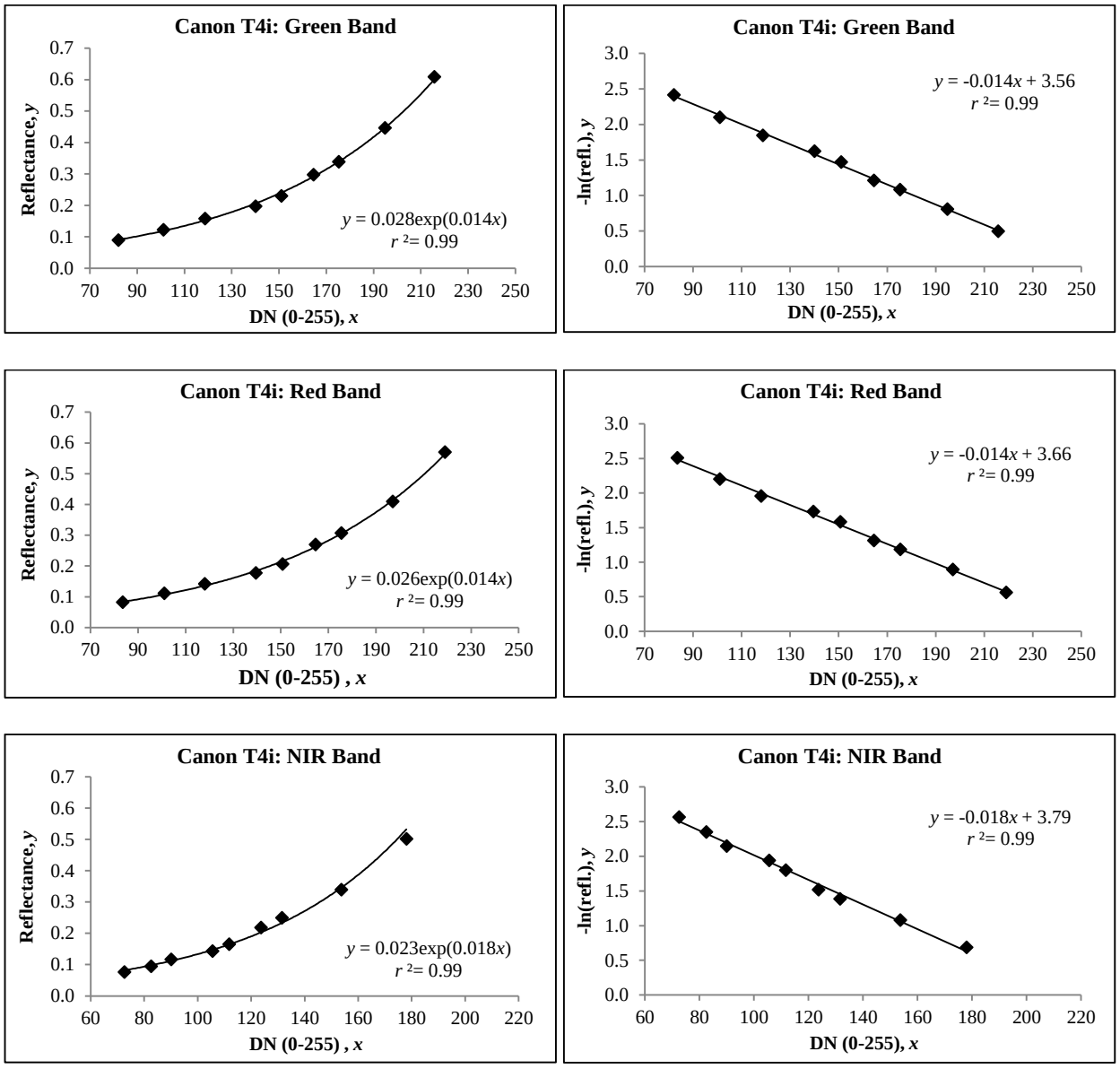

(a) (b)

Figure 6. (a) The relationship between image raw DN (*x*-axis) and mean reflectance of the gray gradient calibration panel (*y*-axis) for each sensor waveband. Each data point represents one gray level; (b) The relationship between image raw DN (*x*-axis) and natural log-transformed reflectance value (*y*-axis) of the gray gradient calibration panel for each sensor waveband. Each data point represents one gray level.

The final step is to build an empirical line calibration equation for every single band image, and then use the equation to convert pixel raw DNs to reflectance. The constant calibration parameter for each waveband is already known. We just need to create another data point using the mean DN of the calibration target as the *x*-coordinate value and the negative natural log-transformed mean reflectance of the target as the *y*-coordinate value. For illustration, the constant calibration parameter for the NIR band of the modified Canon T4i digital camera is 3.79 (Point A). Suppose the mean DN of the calibration target extracted from the NIR band image is 150 and the negative natural log-transformed mean reflectance of the target is 1.45. Therefore, the second point in the coordinate system

will be (150, 1.45) (Point B). The slope *m* of the empirical line calibration equation can be calculated using the following equation:

$$m = \frac{B_y - A_y}{B_x}$$

where A_y is the constant calibration parameter, B_x is the *x* value of Point B, and B_y is the *y* value of Point B. Given the values in the example above, the slope *m* is -0.0156. The calibration equation for the NIR band image is:

$$-\ln(refl.) = -0.0156 \times DN + 3.79$$

This calibration equation will be applied to the entire NIR band image and convert image raw DNs into natural log-transformed reflectance values. These values will then be converted back to reflectance by taking exponential term. The same process needs to be repeated for the green and red band images in order to implement the whole calibration procedure for every CIR image.

METHOD VERIFICATION

This method was verified in the Tallgrass Prairie National Preserve in Chase County, Kansas, on August 21, 2013. In this verification process, we will compare the measured reflectance of tallgrass sampling quadrats with predicted reflectance calculated using this simplified empirical line calibration method described above. A non-parametric Mann-Whitney *U* test will be used to test the null hypothesis (H_0) that there is no difference between the measured and predicted reflectance values of all the sampling quadrats.

A total of 13 sampling frames made of PVC pipes were placed along a straight transact at an interval of approximate 5 meters. Four 0.6 m × 0.6 m (24" × 24") 50% gray calibration targets were distributed in the field next to sampling frames. The sUAS imagery of tallgrass sampling quadrats, together with calibration targets, were acquired at a fixed altitude of 20 m above the ground.

Ten spectral measurements of each sampling quadrat were taken by the spectroradiometer from different viewing angles simultaneously when sUAS images were being acquired. The measured mean reflectance and the mean DNs of each sampling quadrat were both calculated. The mean reflectance of each target at the wavelengths of each sensor waveband was determined beforehand (Table 4). Calibration targets pixels were extracted from each single band image and their mean DNs were also calculated (Table 4).

Table 4. Mean reflectance and mean DN of calibration targets at wavelengths of each sensor waveband.

Band	Target 1		Target 2		Target 3		Target 4	
	Reflectance	**DN**	**Reflectance**	**DN**	**Reflectance**	**DN**	**Reflectance**	**DN**
Green	0.248 (1.39)*	151	0.243 (1.41)*	148	0.251 (1.38)*	155	0.246 (1.40)*	150
Red	0.229 (1.47)*	150	0.227 (1.48)*	146	0.230 (1.47)*	153	0.226 (1.49)*	150
NIR	0.197 (1.62)*	112	0.195 (1.63)*	110	0.199 (1.61)*	114	0.196 (1.63)*	111

* Values in parentheses are negative natural log-transformed reflectance.

One empirical line calibration equation for every single band image was built using the constant calibration parameter as one data point, and the negative natural log-transformed mean reflectance of the calibration target (*y*-coordinate value) and its mean DN (*x*-coordinate value) as another point. The mean DN of each sampling quadrat was then calculated and brought into the corresponding calibration equation to compute the predicted mean reflectance value. All the measured and predicted reflectance values of 13 sampling quadrats for all three bands are shown in Table 5.

The Mann-Whitney *U* test is then performed to study if the difference between measured and predicted reflectance values is statistically significant. The smaller value of the two computed *U* statistics is tested against the critical value (U_c) at a significance level of 0.05, which is 45 for a sample size of 13 in a two-tailed test, and then accordingly accept or reject H_0 based on its *p*-value. All the computed *U* statistics and the test results are presented

in Table 5. As the *p*-values suggest, none of the test results is significant at the 95% confidence level. We fail to reject H_0 and therefore conclude that there is no statistically significant difference between the measured and predicted reflectance values for all the 13 sampling quadrats. It proves that this simplified empirical line method is feasible for calibrating very high spatial resolution sUAS imagery in this study.

Table 5. The Mann-Whitney *U* test between measured and predicted reflectance of thirteen sampling quadrats for each camera waveband.

Quadrat	Green band				Red band				NIR band			
	Measured	**Predicted**	U_1	U_2	**Measured**	**Predicted**	U_1	U_2	**Measured**	**Predicted**	U_1	U_2
1	0.079	0.073			0.057	0.062			0.361	0.352		
2	0.067	0.071			0.052	0.057			0.378	0.366		
3	0.062	0.066			0.057	0.053			0.246	0.254		
4	0.070	0.067			0.058	0.055			0.323	0.336		
5	0.066	0.074			0.061	0.067			0.358	0.351		
6	0.058	0.064			0.048	0.052			0.282	0.290		
7	0.070	0.073	91.5	77.5	0.054	0.051	88	81	0.297	0.291	86	83
8	0.090	0.086			0.052	0.056			0.457	0.468		
9	0.094	0.098			0.079	0.085			0.348	0.342		
10	0.073	0.075			0.066	0.072			0.261	0.257		
11	0.094	0.099			0.082	0.085			0.346	0.336		
12	0.067	0.065			0.060	0.056			0.223	0.228		
13	0.078	0.071			0.069	0.063			0.313	0.327		
	Z-score		-0.333^{ns}		*Z*-score		-0.154^{ns}		*Z*-score		-0.051^{ns}	
	p-value		0.741		*p*-value		0.881		*p*-value		0.960	

Note: The superscript *ns* implies that the difference between the measured and predicted reflectance value is not significant at the 95% confidence level.

DISCUSSION

The empirical line method of radiometric calibration presented in this research is different from those mentioned before (Smith and Milton, 1999; Dwyer *et al.*, 1995; Farrand *et al.*, 1994; Stow *et al.*, 1996), and we believe this method has been greatly simplified for sUAS-based remote sensing from three aspects. First, this is the first study that discovers the relationship between digital image signals collected by a modified commercial DSLR camera and surface reflectance. This type of sensor has been popularly used in sUAS-based remote sensing applications. Second, we have discovered that the relationship between image raw DN and surface reflectance for this particular sensor is not always linear, but exponential as suggested by this study. Third, we have developed a systematic and feasible method to build empirical line calibration equations by using only one gray calibration target, instead of two or more targets, which has dramatically simplified the procedure and reduced the workload in the field.

It is necessary to notice that although our target surface is made of a material that is highly Lambertian, it still does not equally reflect incoming solar radiation of different wavelengths (Figures 1 & 2). It reflects more energy in the visible region than the NIR region of the spectrum. It therefore requires that one calibration equation has to be built for every single band image. Although it increases image processing workload, the calibration accuracy would be highly improved.

Although we consider the reflectance of a calibration target does not change in a short time period, image DNs of a target do change as the weather, atmospheric condition or the Earth-Sun geometry changes. All these external environment factors may influence the slope coefficient of the empirical line calibration equation, but not the *y*-intercept because the *y*-intercept value can be interpreted as the minimum amount of reflectance from the ground that can be detected by the sensor, which is an inherent property of the sensor. It is also worth noting that the empirical line calibration equations developed here are only for the specific sensor being used in this study. We have to admit that the calibration parameters do vary for different sensors. Therefore a calibration equation has to be built and the *y*-intercept calibration parameter has to be calculated for each sensor waveband using the gray gradient panel before data collection. Moreover, although we assume the *y*-intercept calibration parameter and the mean reflectance of a calibration target remain constant in a short time, in reality they do change in a long time period as the instrument and the paint coat are both subject to ageing and degradation. The target surface can also easily get scratched in the field that would damage its Lambertian property. We would therefore suggest to re-paint the target,

re-measure its mean reflectance, and re-determine the constant calibration parameter periodically using the gray gradient calibration panel.

It is also important to note that the mean reflectance of a gray calibration target being used should be greater than the maximum possible reflectance of target area of interest over the spectral region of each sensor waveband. The purpose is to improve prediction accuracy when all the points fall within the confident data range that has been established. This calibration method is therefore more effectively implemented for a land cover type that is relatively homogenous, such as grassland, cropland, and forest, because the maximum possible reflectance of ground objects can be more easily estimated.

The size of a calibration target does matter because it has to be large enough to be seen in the image. It is suggested that the target should be at least several times larger than the sensor ground field-of-view (Smith and Milton, 1999). Since a sUAS can normally fly at different altitudes during one overflight, the sensor field-of-view is difficult to be determined at real time. Our field experience suggests that depending on the image spatial resolution, the side of the square calibration target has to be a least ten times larger than the maximum possible pixel size in order for the targets to be detected from the image. As described by the FAA rules, the legal upper limit flight altitude of a civil sUAS in the United States is 400 ft above the ground. The spatial resolution is about 2.2 cm for a Canon T4i image collected at that altitude, so we would recommend the side of a calibration target has to be at least 22 cm.

SUMMARY

sUAS has become a very popular platform to collect very high resolution remotely sensed imagery for many civilian and scientific applications. Although the sUAS flight altitude is much lower than satellites and piloted aircrafts, atmospheric absorption and scattering issues always exist. In order to perform biophysical analysis, change detection across date, or comparison across sensor using sUAS imagery, radiometric calibration is the foremost step of digital image processing. This research fills the gap through developing a systematic, feasible and convenient method to perform radiometric calibration for remotely sensed data collected by a modified ordinary digital camera using sUAS as the platform.

We have discovered that the relationship between image raw DN and natural log-transformed surface reflectance is linear. The *y*-intercept of the empirical line calibration equation can be interpreted as the minimum surface reflectance that a sensor can detect, which can be used as a constant calibration parameter that does not change as the external environmental conditions change in a short time period. Another data point in the calibration empirical line can be created using the mean DN of a gray calibration target as the *x*-coordinate and its negative natural log-transformed mean reflectance as the *y*-coordinate value. One calibration equation has to be built for every single band image as the weather condition can constantly change during the overflight. The material used to construct the calibration target is the Masonite hardboard with a rough surface that has a highly Lambertian property.

Unlike the radiometric calibration procedure of satellite imagery or the traditional empirical line technique, this method is novel in that it directly converts raw, unprocessed image data to surface reflectance values. The method theory developed in this study can be effectively employed for other sUAS-based remote sensing applications.

ACKNOWLEDGMENTS

We would like to thank the Nature Conservancy and the Tallgrass Prairie National Preserve for providing facilities and access to field sites during this project.

REFERENCES

Barnard, J. 2010. Use of unmanned air vehicles in oil, gas and mineral exploration activities. Paper presented at the *AUVSI Unmanned Systems North America Conference*, Denver, CO, USA, Aug. 24-27, 2010.

Beard, R. W., T. W. McLain, D. B. Nelson, D. Kingston, and D. Johanson. 2006. Decentralized cooperative aerial surveillance using fixed-wing miniature UAVs. *Proceedings of the IEEE*, 94(7): 1306-1324.

Ben-Dor, E., F. A. Kruse, A. B. Lefkoff, and A. Banin. 1994. Comparison of three calibration techniques for utilization of GER 63-channel aircraft scanner data of Makhtesh Ramon, Negev, Israel. *Photogrammetric Engineering and Remote Sensing*, 60(11): 1339-1354.

Bland, G., P. Coronado, T. Miles, P. Bretthauer, A. Lunsford, and J. Bognar. 2004. “Sensors with Wings” – Small UAVs for Earth Science. In *AIAA 3rd “Unmanned Unlimited” Technical Conference, Workshop and Exhibition*, Chicago, IL, USA, Sept. 20-23, 2004.

Dwyer, J. L., F. A. Kruse, and A. B. Lefkoff. 1995. Effects of empirical versus model-based reflectance calibration on automated analysis of imaging spectrometer data: a case study from the Drum Mountains, Utah. *Photogrammetric Engineering and Remote Sensing*, 61(10): 1247-1254.

Everaerts, J. 2008. Unmanned Aerial Vehicles for Photogrammetry and Remote Sensing. In *Advances in Photogrammetry, Remote Sensing and Spatial Information Sciences: 2008 ISPRS Congress Book*, 7: 117-124. CRC Press.

Farrand, W. H., R. B. Singer, and E. Merényi. 1994. Retrieval of apparent surface reflectance from AVIRIS data - a comparison of empirical line, radiative-transfer and spectral mixture methods. *Remote Sensing of Environment*, 47(3): 311-321.

Ferrier, G., and Wadge, G. 1996. The application of imaging spectrometry data to mapping alteration zones associated with gold mineralization in southern Spain. *International Journal of Remote Sensing*, 17(2): 331- 350.

Honkavaara, E., T. Hakala, J. Peltoniemi, J. Suomalainen, E. Ahokas, and L. Markelin. 2010. Analysis of properties of reflectance reference targets for permanent radiometric test sites of high resolution airborne imaging systems. *Remote Sensing*, 2(8): 1892-1917.

Hunt, E. R., W. D. Hively, S. J. Fujikawa, D. S. Linden, C. S. Daughtry, and G. W. McCarty. 2010. Acquisition of NIR-green-blue digital photographs from unmanned aircraft for crop monitoring. *Remote Sensing*, 2(1): 290-305.

Kruse, F. A., K. S. Kierein-Young, and J. W. Boardman. 1990. Mineral mapping at Cuprite, Nevada with a 63-channel imaging spectrometer. *Photogrammetric Engineering and Remote Sensing*, 56: 83-92.

Laliberte, A. S., M. A. Goforth, C. M. Steele, and A. Rango. 2011. Multispectral remote sensing from unmanned aircraft: Image processing workflows and applications for rangeland environments. *Remote Sensing*, 3(11): 2529-2551.

Martin, S., J. Bange, and F. Beyrich. 2011. Meteorological profiling of the lower troposphere using the research UAV “M^{2}AV” Carolo. *Atmospheric Measurement Techniques*, 4(4): 705-716.

Merino, L., F. Caballero, J. Ramiro Martínez-de-Dios, I. Maza, and A. Ollero. 2012. An unmanned aircraft system for automatic forest fire monitoring and measurement. *Journal of Intelligent & Robotic Systems*, 65(1-4): 533-548.

Nebiker, S., A. Annen, M. Scherrer, and D. Oesch. 2008. A light-weight multispectral sensor for micro UAV - Opportunities for very high resolution airborne remote sensing. *The International Archives of the Photogrammetry, Remote Sensing and Spatial Information Sciences*, 37(B1): 1193-1199.

Price, R., C. D. Anger, and S. Mah. 1995. Preliminary evaluation of casi preprocessing techniques. In *Proceedings of the 17th Canadian Symposium on Remote Sensing*, pp. 694-697, 1995.

Stow, D., A. Hope, A. T. Nguyen, S. Phinn, and C. A. Benkelman. 1996. Monitoring detailed land surface changes using an airborne multispectral digital camera system. *IEEE Transactions on Geoscience and Remote Sensing*, 34(5): 1191-1203.

Smith, G. M., and Milton, E. J. 1999. The use of the empirical line method to calibrate remotely sensed data to reflectance. *International Journal of Remote Sensing*, 20(13): 2653-2662.

Van der Meer, F. 1994. Extraction of mineral absorption features from high-spectral resolution data using non-parametric geostatistical techniques. *International Journal of Remote Sensing*, 15(11): 2193-2214.

Veenstra, T. S. and Churnside, J. H. 2012. Airborne sensors for detecting large marine debris at sea. *Marine Pollution Bulletin*, 65(1-3): 63-68.

Wang, C., K. P. Price, D. Van der Merwe, N. An, and H. Wang. 2014. Modeling above-ground biomass in tallgrass prairie using ultra-high spatial resolution sUAS imagery. *Photogrammetric Engineering & Remote Sensing*, 80(12): 1151-1159.